Large Aperture "Photon Bucket" Optical Receiver Performance in High Background Environments

V. Vilnrotter¹, D. Hoppe Jet Propulsion Laboratory, California Institute of Technology 4800 Oak Grove Drive Pasadena, CA 901109 818-354-2745

Victor.A.Vilnrotter@jpl.nasa.gov

Abstract— The potential development of large aperture groundbased "photon bucket" optical receivers for deep space communications, with acceptable performance even when pointing close to the sun, is receiving considerable attention. Sunlight scattered by the atmosphere becomes significant at micron wavelengths when pointing to a few degrees from the sun, even with the narrowest bandwidth optical filters. In addition, high quality optical apertures in the 10-30 meter range are costly and difficult to build with accurate surfaces to ensure narrow fields-ofview (FOV). One approach currently under consideration is to polish the aluminum reflector panels of large 34-meter microwave antennas to high reflectance, and accept the relatively large FOV generated by state-of-the-art polished aluminum panels with rms surface accuracies on the order of a few microns, corresponding to several-hundred micro-radian FOV, hence generating centimeterdiameter focused spots at the Cassegrain focus of 34-meter Assuming pulse-position modulation (PPM) and Poisson-distributed photon-counting detection, a "polished panel" photon-bucket receiver with large FOV will collect hundreds of background photons per PPM slot, along with comparable signal photons due to its large aperture. It is demonstrated that communications performance in terms of PPM symbol-error probability in high-background high-signal environments depends more strongly on signal than on background photons, implying that large increases in background energy can be compensated by a disproportionally small increase in signal energy. This surprising result suggests that large optical apertures with relatively poor surface quality may nevertheless provide acceptable performance for deep-space optical communications, potentially enabling the construction of cost-effective hybrid RF/optical receivers in the future

TABLE OF CONTENTS

1. Introduction	1
2. SOURCES OF OPTICAL INTERFERENCE	2
3. SIGNAL DISTRIBUTION IN THE FOCAL-PLANE	3
4. PERFORMANCE OF FOV-OPTIMIZED PHOTON-BU	JCKET
Receiver	5
5. TELESCOPE APERTURE AND FIELD-OF-VIEW	
CONSIDERATIONS	6
5. SUMMARY AND CONCLUSION	8
REFERENCES	9
RIOGRAPHIES	9

1. Introduction

In this paper we consider design options for large area "photon-bucket" style optical receivers, defined as having fields-of-view (FOV) much greater than the diffraction limit, and employing photon-counting arrays to detect and spatially process the received signals. Large optical "photon-bucket" receivers incorporated into the Deep-Space Network's (DSN's) 34-meter antennas are currently being considered for future deep-space communications applications. One approach proposes to polish the RFreflecting inner solid panels of the DSN's 34-meter antennas to reflect near-infrared wavelengths in the 1064-1550 nanometer range, or if the surfaces of the existing panels prove to be inadequate for near-IR operation replacing them with higher-quality aluminum panels, thus enabling the collection of optical signals without degrading their X-band (8.4 GHz) performance. The system concept for these polished-panel options is shown in Fig. 1. The optical communications receiver assembly will be located near the first available focal-spot F1, next to the input to the beam waveguide on the main reflector, and in the shadow of the subreflector to minimize signal blockage. This placement requires an RF/Optical dichroic mirror that reflects optical but transmits RF wavelengths, which in principle can be implemented as a dielectric-coated pellicle, similar to commercial pellicle reflectors currently available in large sizes (up to 40" diameter). The reflected light is filtered using a narrowband optical filter to minimize background: at 1550 nm, filter bandwidths of 2 Angstroms are feasible, with peak transmissions of approximately 80%.

¹ The authors are with the Jet Propulsion Laboratory, California Institute of Technology

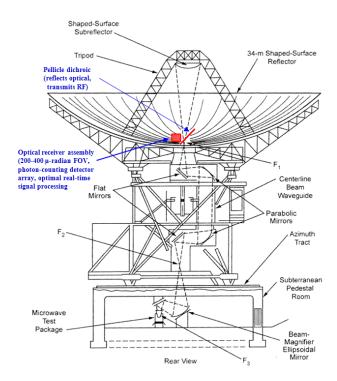


Figure 1. Optical communications receiver assembly placed at F1: RF/Optical dichroic, optical filter, detector array and high-speed signal-processing equipment.

A functional block diagram of the photon-bucket optical receiver assembly is shown in Fig. 2, including the pellicle dichroic designed to reflect optical fields while transmitting RF carriers at X-band (8.4 GHz) to Ka-band (32 GHz) and higher frequencies.

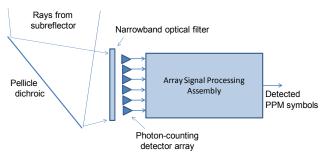


Figure 2. Functional block diagram of the Optical Receiver Assembly, placed on the main reflector near the entrance to the RF beam waveguide in a DSN 34-meter antenna.

The narrowband optical filter is designed to have the narrowest bandwidth consistent with 80% or higher transmission, currently on the order of 2 nanometers (nm). The photon-counting array must be large enough to collect signal energy consistent with the FOV-optimization technique described in [1], roughly matched to the extent of the PSF generated by the polished panels of the photon-bucket receiver. The spatially filtered optical signal is assumed to be processed according to the maximum likelihood detection algorithm, which is designed to achieve

the minimum probability of error consistent with the background environment.

2. SOURCES OF OPTICAL INTERFERENCE

Due to its inherently large FOV, photon-bucket optical receivers are more susceptible to background interference than diffraction-limited receivers, however large area diffraction-limited telescopes are extremely costly and difficult to operate, requiring complex adaptive optics to counter the effects of atmospheric turbulence. Without the use of adaptive optics, turbulence-limited receiver FOV tends to be around 2 arc-seconds (10 micro-radians) during daytime hours when seeing conditions are good, but could be as high as 5 arc-seconds (25 micro-radians) in extreme turbulence.

However, even 25 micro-radian FOV is difficult to achieve with a large-area optical receiver, requiring the use of thick and heavy glass or aluminum panels to attain the desired surface accuracy. With thin and light aluminum panels comparable in cost and weight to standard DSN RF panels, 100-1000 micro-radian fields-of-view appear to be more practical. Therefore we shall concentrate on this region of practically attainable fields-of view, and examine design options to mitigate background interference in large-area photon-bucket optical receivers.

Although bright stars or planets within the receiver's FOV can generate significant background counts at night, the dominant source of intense background interference is the bright sky during daytime, particularly when pointing close to the sun. Scattered solar energy impinging on the focal-plane from the distributed sky background is characterized by the sky spectral radiance function $\mathcal{N}(\lambda)$, which has units of watts per collecting area A (in meters), solid-angle field-of-view Ω (in steradians), and filter bandwidth $\Delta\lambda$ (in nanometers), at a given wavelength λ . An example of sky radiance as a function of wavelength in a desert environment such as Goldstone, CA, is shown in Fig. 3. Spectral radiance is a strong function of distance from the sun, and may increase significantly if the receiver is pointed close to The sun.

The average background power impinging on the detector array in the receiver's focal-plane can therefore be expressed as $P = \eta_{opt} \mathcal{N}(\lambda) A\Omega \Delta \lambda$ in units of watts, where η_{opt} is the throughput of the optical system including reflectivity of the main reflector, subreflector and dichroic, as well as the transmission of the narrowband optical filter.

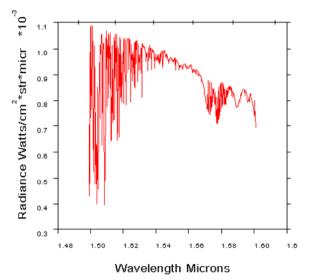


Figure 3. Example of sky radiance for a desert model, at a "sun-earth-probe" (SEP) angle of 10 degrees.

It is convenient to express Ω in terms of the radius R of a circular area in the focal-plane, at an effective focal-distance f_{eff} from the main reflector: $\Omega = \pi R^2 / f_{eff}$. Taking into account the detection efficiency of the array, η_d , the average number of photo-counts per second generated by an array of radius R can be expressed as $n_b = \eta_{opt} \eta_d \ \pi \ R^2 \mathcal{N}(\lambda) A \Delta \lambda / h \nu \ f_{eff}$, where h is Planck's constant and $\nu = c/\lambda$ is the center frequency of the narrowband optical filter. Therefore, the average number of photon-counts observed in a time-interval τ by a detector array of radius R is given by the expression

$$K_{b} = \eta_{opt} \eta_{d} \mathcal{N}(\lambda) A \Omega \Delta \lambda \tau / h v$$

$$= A \eta_{opt} \eta_{d} \pi R^{2} \mathcal{N}(\lambda) \Delta \lambda \tau / h v f_{eff} \equiv I_{b} A$$
(1)

in terms of both solid-angle field-of-view Ω and detectorarray radius R. I_b represents the average background photon-count per unit aperture collecting area, impinging on the detector array of radius R. These expressions will be useful in modeling and evaluating photon-bucket receiver performance in the presence of intense background.

In addition to background radiation dust, scratches, and high-order surface roughness on the polished panel surfaces leads to scattering of sunlight into the receiver FOV and optical filter bandwidth, which also has to be taken into account when pointing close to the sun. Since every panel contributes to surface scattering, the total amount of surface-scattered background, when present, depends on the area of the polished-panel collecting aperture.

3. SIGNAL DISTRIBUTION IN THE FOCAL-PLANE

To motivate the two-dimensional Gaussian model for the focal-plane signal distribution, we consider a realistic example of the point-spread-function (PSF) generated by a high-quality aluminum panel.

Typical FOV's obtained by state-of-the-art aluminum panels can be calculated using a surface model that corresponds to realistic rms surface errors and spatial distributions. This approach was used to generate the expected FOV for a high quality but realistic polished aluminum panel, showing that approximately 50% of energy falls within about 225 μ rad (Fig. 4), but also indicating the presence of narrower "hot-spots" that can lead to further improvements in communications performance when processed with a photon-counting detector array.

In practice, the 50% FOV will be larger than 225 µrad because of the tilt between the panels and the effect of the atmospheric turbulence. Better panel manufacturing practices, combined with precise panel alignment implementation can improve the FOV, potentially increasing cost. Ultimately, cost is a tradeoff between detector size, observed sky background light, stray light, panel surface quality, and panel alignment accuracy.

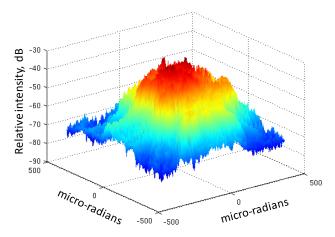


Figure 4. Example of PSF generated by a realistically modeled panel surface error distribution, showing high concentration of signal energy in the inner +/- 120 micro-radians from center. Horizontal axes in μ rads, vertical axis in dB (intensity, arbitrary units)

With the relatively large field-of-view (FOV) of polishedpanel optics, which are not intended to be diffractionlimited but rather intended to operate in "photon-bucket" mode with much greater than diffraction-limited FOV, the focused laser signal at F1 will have to be detected with large-area photon-counting detectors since the bell-shaped point-spread-function (PSF) diameter *d* at F1 is given by the expression $d = FOV \times f_{\it eff}$, where $f_{\it eff}$ is the effective focal-length of the Cassegrain optical system, in this case $f_{\it eff} \cong 100$ meters. For example, if the FOV is 225 microradians, then at F1 the PSF diameter is approximately $d = (2.25 \times 10^{-4}) \times 100 = 2.25$ cm, requiring a large-area photon-counting detector array to capture most of the signal energy.

To facilitate analysis, the detector plane is modeled as a large array of small detector elements (or subarrays), essentially covering the extent of the PSF plus any uncertainty in its center coordinates before spatial acquisition (centering) has taken place. The key elements of the detector-plane model are shown in Fig. 5, assuming that enough spatial modes are impinging on each detector element to justify the constant PSF intensity assumption.

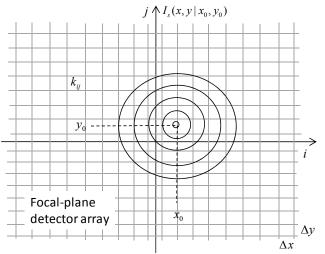


Figure 5. Detector-plane model of photon-counting array and PSF with small pointing offsets.

For the purposes of analysis, the PSF is assumed to be a two-dimensional Gaussian distribution with center at (x_0, y_0) and intensity distribution

$$I_s(x, y \mid x_0, y_0) = I_s (2\pi \sigma_s^2)^{-1} \times \exp\{-[(x - x_0)^2 + (y - y_0)^2]/2\sigma_{PSF}^2\}$$
 watts/cm^{{2})

The detector elements are taken to be small squares in this model, with power P_{ij} over the ij th detector-element equal to the integral of the intensity distribution over its active area:

$$P_{s}(i, j \mid x_{0}, y_{0}) = \int_{(i-1/2)\Delta}^{(i+1/2)\Delta} dx \int_{(j-1/2)\Delta}^{(j+1/2)\Delta} dy I_{s}(x, y \mid x_{0}, y_{0})$$

$$\cong \Delta^{2} I_{s}(i\Delta, j\Delta \mid x_{0}, y_{0})$$

Integrating power over time yields energy, or average

"count-intensity" λ_s if the received laser energy is measured in terms of photons:

$$\lambda_s(i,j \mid x_0, y_0) = \int_0^T P_s(i,j \mid x_0, y_0) dt$$

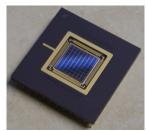
$$\cong T\Delta^2 I_s(i\Delta, j\Delta \mid x_0, y_0)$$
(4)

With this model, the photon count from the *ij*-th detector element over a time interval of T seconds is a Poisson distributed random [2] variable with count probability:

$$p(k_{ij} \mid x_0, y_0) = [\lambda_s(i, j \mid x_0, y_0)]^{k_{ij}} \times \exp[-\lambda_s(i, j \mid x_0, y_0)]/k_{ij}!$$
(5)

where we have assumed for now that background photons are negligibly small.

The focused laser signal will be detected with photoncounting detectors for best direct-detection performance, however large-area photon-counting detectors are still in the research and development phase and hence not readily available at the near-IR wavelengths of 1064 and 1550 nm. Since the numerical aperture (NA) of the light-cone reflected from the polished subreflector is approximately 0.14, it is clear that the spotsize at F1 can be further reduced via optics at the cost of increasing its NA, from 2-3 cm to about 1 cm: this reduction could enable the use of large-area Geiger-mode Avalanche Photodiode (GAPD) detectors combined with fiber waveplates to efficiently guide the light to the detector's active areas. An example of an 8X8 mm photon-counting detector array currently under development at aPeak, Inc. (Massachussetts) suggests that large area detector arrays can be developed with quantum efficiencies (QE) in the neighborhood of 50%, to accommodate cm-size spots generated by large photon-bucket optical receivers. Examples of large-area GAPD arrays with various matching fiber-plate configurations currently under development at aPeak Inc. operating at 1064 nm, are shown in Fig. 6.



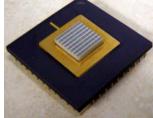


Figure 6. a) 8X8 mm GAPD array, with b) matched fiber-optic plate, converting a large signal distribution to a smaller detector array. (Courtesy aPeak, Inc. Waltham, Massachussetts)

Photon-counting detection is followed by high-speed digital signal processing, which extracts angle-of-arrival

information and temporal synchronization from the array of counts, centering the PSF over the detector array and keeping the PPM slots synchronized with the receiver clock. After successful spatial and temporal acquisition, the receiver is ready to carry out its primary mission, that is, the detection of high-speed information contained in the optical signal received from the optical transmitter aboard the spacecraft. For a ground-based receiver, operating during daytime and occasionally pointing close to the sun, it is imperative that the receiver field-of-view be optimized, to achieve best performance under all possible operating conditions ranging from night-time to small Sun-Earth-Probe (SEP) angles.

4. PERFORMANCE OF FOV-OPTIMIZED PHOTON-BUCKET RECEIVER

Following successful spatial and temporal acquisition, essentially driving any initial offset (x_0, y_0) to zero, the PSF is kept centered over the detector array by means of a closed-loop tracking circuit. Temporal acquisition and tracking keeps the receiver clock synchronized with the slot-boundaries. Under these conditions, the receiver FOV can be optimized to achieve best detection performance by increasing the acceptance-angle of the receiver in small increments, and computing the PPM symbol-error probability for each increasing radius R in the detector-plane [3].

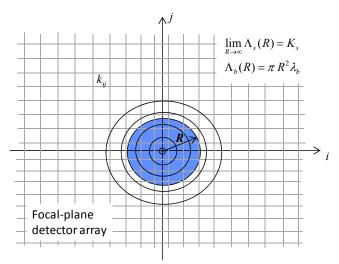


Figure 7. Optimization of receiver FOV by increasing the radius of the acceptance-disk in the detector plane until the minimum PSE is reached.

The amount of signal energy collected by a circular FOV of radius was calculated as:

$$\frac{1}{2\pi\sigma_s^2} \int_0^R 2\pi r \exp[-r^2/2\sigma_s^2] dr = -\int_0^R \frac{r}{\sigma_s^2} \exp[-r^2/2\sigma_s^2] dr$$
$$= \exp[-r^2/2\sigma_s^2] \Big|_0^0 = 1 - \exp[-R^2/2\sigma_s^2]$$

In the limit as R approaches infinity all of the signal energy is captured, according to the Gaussian PSF model illustrated in Fig. 7. Therefore, $\lim_{R \to \infty} \Lambda_s(R) = K_s$, where K_s is the

total signal energy per pulse, measured in terms of photon energy, passing through the receiver aperture. The background photon distribution is assumed to be uniform in the detector-plane, hence the collected background energy increases with R in proportion to the area of the circular FOV, hence there is no limit to the amount of background energy that can be collected by the receiver according to this model: $\Lambda_b(R) = \pi R^2 \lambda_b$, where λ_b is the average background photon-count per square centimeter in the detector-plane.

Consider the probability of correct symbol detection, with PPM signaling. For any R, the probability of correct symbol detect ion is at least as great as the probability that the photon-count in the correct slot containing the signal-pulse, exceeds the count in every other slot: to be precise, tying equalities in (r-1) noise-slots (1 < r < M) should also be considered, resolved by tossing a fair r-sided die, but with high average signal and background energies these events have extremely small probabilities, hence can be neglected. With this approximation, the lower bound on the probability of correct decision, $P_M^l(C)$, as a function of R is given by:

$$P_{M}^{I}(C) \ge \sum_{k=1}^{\infty} \frac{\left(\Lambda_{s}(R) + \Lambda_{b}(R)\right)^{k}}{k!} \exp\left[-\left(\Lambda_{s}(R) + \Lambda_{b}(R)\right)\right] \times \left\{\sum_{j=0}^{k-1} \frac{\left(\Lambda_{b}(R)\right)^{j}}{k!} \exp\left[-\left(\Lambda_{b}(R)\right)\right]\right\}^{M-1}$$
(5)

$$P_M^u(E) \equiv 1 - P_M^l(C) \ge P_M(E) \cong P_M(E)$$

The corresponding symbol error probability, $P_{M}(E)$, is actually somewhat less than predicted by equation (5), but not significantly so. For high background cases, the Poisson computations are time-intensive, in which case a much faster Gaussian approximation can be used. The approximate Gaussian formula replaces the Poisson probabilities with continuous Gaussian densities with matched second-order statistics, yielding the following equation for the probability of correct decoding:

$$\begin{split} P_{M}(C) &\cong \int_{-\infty}^{\infty} dy \, Gsn[\Lambda_{s}(R) + \Lambda_{b}(R), y] \times \\ &\left[\int_{-\infty}^{y} dx \, Gsn[\Lambda_{b}(R), x] \right]^{M-1} \end{split} \tag{6}$$

where $GSN(\Lambda,x)$ refers to the Gaussian density of the random variable x with mean and variance Λ . This approximation yields a somewhat pessimistic evaluation of photon-bucket optical receiver error performance, but helps to provide initial insights into the behavior of key design parameters thus reducing the search-space for the more accurate Poisson model.

5. TELESCOPE APERTURE AND FIELD-OF-VIEW CONSIDERATIONS

The average number of background photons collected by the optical receiver depends on the spectral radiance of the extended background which, in turn, depends on how close to the sun the receiver is pointing, the bandwidth of the narrowband optical filter, the optimized FOV of the optical receiver, and the effective area of the collecting aperture. There are several options for recovering receiver performance degradations due to increased background, including the following:

- a) Reducing Optical Filter Bandwidth: Although narrowband optical filters of 2 angstrom bandwidth are challenging to design and stabilize in the 1064-1550 nm wavelength range, they are nevertheless available commercially or as custom designs and can be manufactured to large aperture optical communications requirements. However, there are technological limits to reducing the bandwidth of interference-filters below a certain limit, without incurring large losses in signal throughput. Since we assumed a 2 Angstrom optical filter bandwidth at 1550 nm wavelength with 80% transmission, which is already close to the practical limit with current technology, it is reasonable to assume that significant additional improvements are not likely.
- b) Increasing Signal Power from the Spacecraft: The signal energy reaching the receiver could be increased by increasing the laser power or the transmitter telescope diameter on the spacecraft, but these are generally costly and impractical options.
- c) Increasing Receiver Aperture: A more practical option is to increase the optical receiver diameter on the ground, especially if this increase does not incur unreasonable demands on the antenna's backup structure. Since the polished panel approach essentially replaces the existing aluminum RF panels with higher-quality aluminum polished-panels of approximately the same weight,

the impact on existing 34-m antennas is expected to be minimal. We therefore proceed to analyze the problem of compensating for increased background by increasing the signal energy, simply by adding more panels with similar FOV to increase the effective aperture.

The following system parameters will be assumed in the design examples: 50 cm transmitter optics, 10 watts of laser power exiting the telescope, 26 meter diameter collector corresponding to 531 square meters of aperture, background radiation evaluated at SEP = 10 degrees, PSF diameter of approximately 1 cm at F1, and an optical system throughput of 0.324, which includes main reflector and subreflector reflection losses (90% on each surface), optical filter transmission losses (80% transmission for a 2 Angstrom optical filter), as well as 50% detector quantum efficiency. The modulation is 4-symbol PPM, with slot-duration of 0.5 ns, resulting in 1 GBPS datarate, as in [1].

Contours of constant symbol-error probability PSE in the (K_s, K_b) plane were computed for *PPM* symbols with M = 4, by first computing PSE for increasing K_s with fixed K_b , until the desired symbol-error probabilities of 0.4, 0.1, 0.01 and 0.001 were reached, as shown in Figure 8, computed via Poisson probabilities using equation (5).

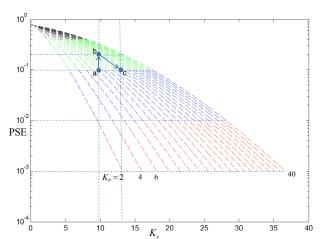


Figure 8. Probability of symbol error, PSE, for M=4 PPM signaling as a function of K_s , for a range of background energies, K_b .

The PSE calculations were carried out for increasing values of average background photon-counts K_b , and the signal photon-counts K_s that achieved the desired PSE were recorded along with K_b , for each of the four symbol-error probabilities, in the range $0 < K_b < 40$. This data was

used to plot the contours of constant-PSE shown in Fig. 9.

Note that for high background intensities, corresponding roughly to $K_b > 10$ in Figure 9, the slopes of the constant-PSE contours are much greater than one, implying that a large increase in background interference can be compensated by a relatively small increase in receiving aperture.

For the following two design examples, we assume that the photon-bucket receiver was designed to operate with M = 4 PPM at an uncoded symbol-error probability of PSE = 0.1, which is capable of attaining mission requirements for coded performance with rate-1/2 codes [1].

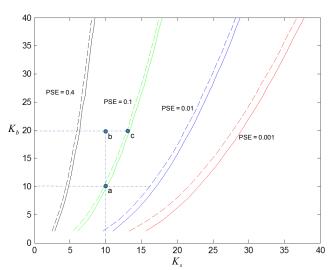


Figure 9. Contours of constant symbol-error probability, PSE, over the (Kb, Ks) plane. Dashed curves were computed using Poisson probabilities, solid curves computed via the faster Gaussian approximation.

Note that increasing the background energy by pointing closer to the sun at constant signal energy results in vertical trajectories in Figs. 8 and 9. For example, starting at an uncoded symbol-error probability PSE = 0.1 and $K_b = 10$ (point "a" in Figs. 8 and 9, $K_b = 10$), then increasing the background to $K_b = 20$ (point "b") detection performance degrades to approximately PSE = 0.2. One way to compensate for this loss and return to the desired PSE of 0.1 is to increase the received signal energy, perhaps by increasing the transmitted power or the gain of the transmitting telescope: although these options are not very practical, the desired performance of PSE=0.1 could be regained along the constant background contours in Figs. 8 and 9, by increasing K_s to 13 (point "c"). The trajectories appear different in the two representations, but the conclusion is the same: excess background can be compensated by a relatively small increase in signal energy. In other words, a 30% increase in signal energy compensates for a 100% increase in background energy due to higher spectral radiance as the receiver points closer to the sun.

Iterative Compensation for Increased Background.

Receiver performance can also be recovered in a practical manner by increasing the receiving aperture, hence collecting more signal energy without increasing transmitter gain or power. Unfortunately, a greater collecting aperture also collects more background energy, hence the initial increase in background cannot be compensated in a single step, as for the case when the transmitted signal power at the spacecraft is increased.

The contour corresponding to PSE = 0.1 was re-plotted in Fig. 10, to help visualize the concept of increasing the aperture incrementally to compensate for an increase in background energy possibly resulting from pointing the receiver closer to the sun at some future time, or perhaps by a bright planet (such as Mars) entering the receiver's FOV. The following derivation illustrates how excess background intensity can be compensated for by increasing the collecting area to maintain the desired PSE.

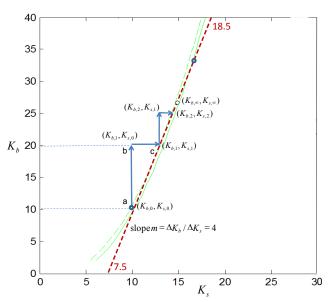


Figure 10. Compensation for excess background by increasing signal energy via aperture expansion, with the goal of maintaining uncoded symbol-error probability of PSE = 0.1.

We start by assuming that the initial operating point was $(K_s = 10, K_b = 10)$ at point "a", but that sometime later the background doubled, moving the operating point to $(K_{s,0} = 10, K_{b,0} = 20)$ corresponding to point "b", perhaps the result of pointing the receiver closer to the sun. Receiver performance clearly degrades due to the increase in background energy (since point "b" is now above the

PSE=0.1 contour, and close to PSE=0.2), the idea is to try to compensate for the increased background by adding more polished panels to increase the collecting aperture and hence the signal energy in order to move the operating point back onto the PSE=0.1 contour.

In order to re-establish the desired receiver performance of PSE=0.1, more signal energy must be supplied, which can be accomplished by adding more polished panels to increase the effective aperture by ΔA square meters, thus capturing a larger fraction of the impinging signal fields according to the equation $\Delta K_{s,1} = I_s \Delta A$, where $\Delta A \equiv A_1 - A_0$, yielding the new operating point $(K_{b,0},K_{s,1})$. However, this leads to a corresponding increase in background energy according to the equation $\Delta K_{b,1} = I_b \Delta A = (I_b/I_s)\Delta K_{s,1}$, where the FOV remains constant since the effective focal-length f_{eff} and detector radius R have not changed. This increase in background energy yields the new operating point $(K_{s,1},K_{b,1})$, which still does not meet symbol-error requirements as can be seen in Fig. 10, hence requires further increases in receiving aperture.

The first iteration yields the new operating points $(K_{s,1}, K_{b,1})$, whose components can be expressed as:

$$K_{s,1} = K_{s,0} + \Delta K_{s,1} = I_s (A + \Delta A_1)$$

$$K_{b,1} = K_{b,0} + \Delta K_{b,1} = I_b (A + \Delta A_1) = \frac{I_b}{I_s} (K_{s,0} + \Delta K_{s,1})$$
(7)

A useful approximate expression can be obtained by finding the tangent to the constant-PSE contour after the first signal increment has been applied, at the point $(K_{s,1}, K_{b,0})$, and using this linear approximation to the constant-PSE contour at the tangent point instead of the exact contour. Assuming that the tangent line at this point has slope m, subsequent incremental increases in K_s can be expressed as:

$$K_{s,2} = K_{s,0} + \Delta K_{s,1} + \frac{I_b}{I_s m} \Delta K_{s,1}$$

$$K_{s,3} = K_{s,0} + \Delta K_{s,1} + \frac{I_b}{I_s m} \Delta K_{s,1} + \left(\frac{I_b}{I_s m}\right)^2 \Delta K_{s,1}$$
(8)

and so on. This leads to the following infinite series for the point of convergence along the K_s axis, denoted as $K_{s,\infty}$:

$$\begin{split} K_{s,\infty} &= K_{s,1} + \Delta K_{s,1} \sum_{k=0}^{\infty} (I_s m / I_b)^{-k} = K_{s,1} + \Delta K_{s,1} (1 - \frac{I_b}{I_s m})^{-1} \\ &= K_{s,1} + \Delta K_{s,1} \, \alpha / (\alpha - 1); \qquad \alpha = I_s m / I_b \end{split}$$

Similarly for
$$K_b$$
: $K_{b\infty} = (I_b / I_s) K_{s\infty}$ (7)

The above analysis is restricted to the range of values

 $\alpha > 1$, since for $\alpha = 1$ the incremental aperture expansion idea does not converge: $\lim \alpha / (\alpha - 1) = \infty$.

In the example illustrated in Fig. 10,

$$K_{b,0}=20,\,K_{s,0}=10,\,\Delta K_{s,1}\cong 3,\,\Delta K_{b,1}\cong 6,\,$$
 $m=40/11=3.64$ and $\alpha/(\alpha-1)=2.22$. The signal and background energies converge to the following final values: $K_{s,\infty}=10+6.67=16.67,\,$ and $K_{b,\infty}=2K_{s,\infty}=33.3,\,$ respectively. With the linear approximation to the PSE-contour in this example the final design point will actually be on a slightly lower-PSE contour, providing a small margin at the receiver against background interference.

The increase in signal energy required to compensate for the 100% increase in background energy is no greater than 67%, representing at most 67% increase in area or 29% increase in receiver diameter. However, as shown in the design example, this approach tends to yield lower PSE than the original design point, which implies that the design point can be reached with even smaller increases in collecting aperture. Adding some more polished panels to the outer ring may therefore be a practical way to accommodate severe increases in background interference, whether the excess background is the result of pointing closer to the sun, or a bright object such as a planet entering the receiver's fields of view.

6. SUMMARY AND CONCLUSION

This paper considered a novel design option for "photon-bucket" type optical communications receivers operating in high background environments, whereby the large fields-of-view characteristic of such receivers is compensated by increasing the collector area. It is shown that with pulse-position modulated signals and photon-counting detection, relatively small increases in collecting area can be used to compensate for increased background, caused possibly by the requirement to point the receiver closer to the sun. Therefore, this approach may provide a cost-effective way to incorporate large-aperture optical receivers directly onto existing 34 meter antennas of the Deep Space Network by replacing some of the RF panels with higher quality polished panels, simultaneous reception of microwave and optical frequencies for future deep-space missions.

Acknowledgment: The research described in this paper was carried out at the Jet Propulsion Laboratory, California Institute of Technology, under contract with the National Aeronautics and Space Administration.

The authors would like to thank Sabino Piazzolla of JPL for determining the effective sky radiance at 10 degrees SEP

angle due to atmospheric scattering, and providing the graph shown in Fig. 3.

REFERENCES

- [1] V. Vilnrotter, "Hybrid RF/Optical Communications via 34-m DSN Antennas," IPN Progress Report 42-181, Jet Propulsion Laboratory, February 15, 2009.
- [2] R. Gagliardi and S. Karp, *Optical Communications*, John Wiley and Sons, New York, 1976.
- [3] V. Vilnrotter, M. Srinivasan, "Adaptive Detector Arrays for Optical Communications Receivers," IEEE Transactions on Communications, Vol. 50, Issue 7, July 2002.

BIOGRAPHIES



Victor A. Vilnrotter (M'79, SM'02) received his Ph.D. in electrical engineering and communications theory from the University of Southern California in 1978. He joined Jet Propulsion Laboratory, Pasadena, CA in 1979, where he is a Principal Engineer in the Communications Architectures and

Research section. His interests include electronic compensation of large antennas with focal-plane arrays, adaptive combining algorithms for large antenna arrays, optical communications through atmospheric turbulence, the application of quantum communications to deep-space optical links, and the development of uplink array calibration and tracking technologies. He has published extensively in conferences and refereed journals, and has received numerous NASA awards for technical innovations.



Daniel J. Hoppe (M'79, SM'00) received the B.S. and M.S. degrees in electrical engineering from the University of Wisconsin Madison in 1982 and 1983, and the Ph.D. degree, also in electrical engineering, from the University of California Los Angeles in 1994. He is currently at the Jet

Propulsion Laboratory where he is a principal engineer. His efforts there involve electromagnetic analysis and design of microwave and optical devices for a number of ground-based and space-based applications. Dr. Hoppe has also been a visiting lecturer at UCLA since 1995. He was awarded the NASA Exceptional Service Medal in 1993, and in 1994 he was recognized as the outstanding Ph.D. student in the School of Engineering and Applied Science at UCLA. Dr. Hoppe is a senior member of the IEEE, and has been awarded several U.S. patents.